Energy Storage Materials 35 (2021) 586–594

Contents lists available at ScienceDirect

Energy Storage Materials

journal homepage: www.elsevier.com/locate/ensm

Ultra-stable and highly reversible aqueous zinc metal anodes with high preferred orientation deposition achieved by a polyanionic hydrogel electrolyte

Jianlong Cong, Xiu Shen, Zhipeng Wen, Xin Wang, Longqing Peng, Jing Zeng*, Jinbao Zhao*

State Key Lab of Physical Chemistry of Solid Surfaces, Collaborative Innovation Center of Chemistry for Energy Materials, State-Province Joint Engineering Laboratory of Power Source Technology for New Energy Vehicle, College of Chemistry and Chemical Engineering, Xiamen University, Xiamen, 361005, China

ARTICLE INFO

Keywords:
Zinc metal anodes
Polyanionic hydrogel electrolyte
Stability
Reversibility
High preferred orientation

ABSTRACT

Although aqueous zinc metal batteries (AZMBs) have attractive advantages such as high safety, low cost and eco-friendliness, severe dendrites formation and side reactions of zinc metal anodes cause a serious challenge for commercial applications. Herein, a polyanionic hydrogel electrolyte, poly 2-acrylamido-2-methyl-1-propane sulfonate zinc (PAMPSZn) is firstly designed and synthesized by ion exchange and free-radical polymerization. The PAMPSZn hydrogel electrolyte owns fixed polyanionic chain and restricted Zn^{2+} transport channels, which can effectively alleviate the side reactions and prevent the formation of Zn dendrites simultaneously. Consequently, the anode-friendly electrolyte not only enables ultra-stable Zn plating/stripping over 4500 h at 1.0 mA cm^{-2}, but also achieves high preferred orientation deposition during the procedure of repeated plating/stripping. It delivers high reversibility with high initial coulombic efficiency (87.5%) and average coulombic efficiency (99.3%) in Zn/Cu cells at 0.5 mA cm^{-2}. Zn/V_2O_5 cells with the developed electrolyte also possess outstanding cycle stability with capacity retention of 80.2% after 400 cycles at 0.5 A g^{-1}. The PAMPSZn hydrogel electrolyte with unique fixed polyanionic chain and restricted Zn^{2+} transport channels demonstrates an effective strategy to solve both dendrites formation and side reactions in AZMBs, providing a new opportunity for high performance AZMBs.

1. Introduction

Recently, lithium ion batteries (LIBs) have been widely used in electric vehicles and portable electronic for their excellent electrochemical performance [1–5]. However, safety problems caused by flammable organic electrolyte drive researchers to develop alternatives to LIBs [6–8]. Among the various next-generation energy storage systems [9–12]. AZMBs were regarded as the most promising candidate because zinc metal anodes possess unique advantages, such as low redox potential (−0.76 V vs. standard hydrogen electrode), high theoretical capacity (820 mAh g^{-1} and 5855 mAh cm^{-3}), good compatibility with aqueous solutions, high safety and environmental friendliness [13–16]. Nonetheless, Zn metal anodes suffer from severe dendrites formation and side reactions with by-products (such $Zn_4(OH)_6SO_4{\cdot}5H_2O$) in the $ZnSO_4$ aqueous electrolyte, leading to poor cycle life and low coulombic efficiency, which has been hindering the commercial application of AZMBs [17–22].

To solve these issues, a lot of effort was devoted to suppressing dendrites formation and alleviating the side reactions. It's an effective way for suppressing dendrites formation to construct an ion modulation layer tuning the diffusion behavior, including TiO_2 layer [23], nanoporous $CaCO_3$ layer [24], multifunctional brightener-inspired layer [25], zeolitic imidazolate frameworks (ZIF-8) [26], zinc-aluminum alloys anodes [27], epitaxial electrodeposition of Zn [28], and so on. In addition, lots of strategies were reported for alleviating the side reactions, such as using $Zn(CF_3SO_3)_2$ electrolyte instead of $ZnSO_4$ electrolyte [29], employing "water-in-salt" electrolytes [30, 31], introducing electrolyte additives [32-34], adopting single ion conductive electrolyte [35, 36], organic electrolyte [37], hydrogel electrolyte [38-43], and solid state electrolyte [44]. However, the life span of the zinc metal anodes achieved by most modification strategies has not yet reached commercial requirements. Dendrites suppression and side reactions inhibition paly an equally important role in long-life AZMBs. To achieve long-life and high reversible AZMBs, dendrites suppression or side reactions inhibition should be considered and resolved at the same time. Reasonable design of electrolyte composition and structure is one of the effective strategies to achieve long-life and highly reversible AZMBs.

Herein, a kind of hydrogel electrolyte whose polyanionic chain is fixed in the hydrogel electrolyte was firstly developed by ion exchange and free-radical polymerization. Free contact between Zn metal anodes

* Corresponding authors.
E-mail addresses: zengjing@xmu.edu.cn (J. Zeng), jbzhao@xmu.edu.cn (J. Zhao).

https://doi.org/10.1016/j.ensm.2020.11.041
Received 13 October 2020; Received in revised form 24 November 2020; Accepted 29 November 2020
Available online 1 December 2020

and $-SO_3^-$ was restricted due to the fixed anion and the fixed polyanionic chain with $-SO_3^-$ induced uniform Zn^{2+} transport channels. As a result, ultra-stable and highly reversible plating/stripping of Zn (over 4500 h operation hours and 99.3% average coulombic efficiency) were achieved in the Zn/Zn symmetric cells and Zn/Cu asymmetric cells, respectively. Meanwhile, the developed electrolyte also achieved the high preferred orientation deposition of Zn^{2+}.

2. Experimental

2.1. Materials

2-Acrylamido-2-methyl-1-propanesulfonic acid (AMPS, 98%), Zinc carbonate basic ($3Zn(OH)_2•2ZnCO_3$, AR), N,N′-Methylenebis(acrylamide) (MBAA, 99%), α-Ketoglutaric acid (α-KGA, 99%) and sulfuric acid ($ZnSO_4$, 99%) were purchased from Aladdin. Zn foils (100 μm in thickness), Cu foils (15 μm in thickness) and Ti foils (50 μm in thickness) were commercialized. V_2O_5 (99.7%) were purchased from Energy Chemical. Glass fiber (about 1 mm in thickness) was purchased from Whatman.

2.2. Preparation of Poly 2-acrylamido-2-methyl-1-propane sulfonate zinc (PAMPSZn)

10.3600 g AMPS and 3.0195 g $3Zn(OH)_2•2ZnCO_3$ were mixed in 25.0 mL deionized water under stirring until no obvious bubbles exist. The suspension was centrifuged to obtain clear solution of Zinc 2-acrylamido-2-methyl-1-propane sulfonate (AMPSZn). Then 0.1542 g MBAA as a cross-linker and 0.0036 g α-KGA as an initiator were added in the solution under stirring for 1 h. The solution was injected into a Teflon mold with a glass cover. The PAMPSZn hydrogel electrolyte (1.0 mm in thickness) was synthesized by irradiating with a UV lamp (wavelength 365 nm) for 1 h. 1.0 M, 2.0 M and 3.0 M (based on the concentration of AMPS monomer) of PAMPSZn hydrogel electrolyte are denoted as PAMPSZn-1, PAMPSZn-2, PAMPSZn-3, respectively.

2.3. Preparation $V_2O_5•1.6H_2O$ cathode materials

$V_2O_5•1.6H_2O$ cathode materials were synthesized successfully by a simple hydrothermal method. 0.35 g V_2O_5 and 2 mL H_2O_2 (30%) were mixed in 30.00 mL deionized water under string for 3 h. The mixture was added into a Teflon autoclave and heated at 200°C for 6 h. The resultant product was collected and freeze-dried.

2.4. Cell assembly

The CR2016 cells were assembled in an air environment and tested for the electrochemical properties by a multichannel battery test system (LAND CT2001A, China). Zn foils were used as anode. The cathode electrodes were prepared by mixing the prepared $V_2O_5•1.6H_2O$ cathode materials, acetylene black and PVDF in a weight ratio of 7:2:1 in NMP solvent, then casting the slurry on Ti foils. The cathode electrodes were dried at 80°C for 12 h in a vacuum oven. The mass loading of the cathode electrodes was about 1.5 mg cm^{-2}. The PAMPSZn hydrogel was cut into slices in 18 mm diameter as electrolyte. As a comparison, the 2.0 M $ZnSO_4$ aqueous electrolyte and glass fiber with a diameter of 18 mm were used as electrolyte and separator, respectively.

2.5. Characterizations

The structure of AMPS and PAMPSZn was analyzed by Fourier transform infrared spectrometer (FTIR, Nicolet iS5, Themor Electro Co., USA). The morphology and energy dispersive spectrometer (EDS) element mapping of the samples was characterized by a field emission scanning electron microscope (SEM, Hitachi S-4800). Transmission electron microscope (TEM, FEI Tecnai F30) was used to observe the morphologies of the cathode materials. Three dimensional morphology and surface roughness were characterized and calculated by confocal laser microscopy (CLMS, VK-X1000, KEYENCE Co.), X-ray diffraction (XRD) patterns of V_2O_5 and Zn anodes, and grazing incidence X-ray Diffraction (GIXRD) patterns of zinc plating/stripping layer were collected by a Rigaku Ultima IV diffractometer (Persee instrument with Cu Kα radiation ($\lambda = 1.5406$ Å)). Raman spectrum was acquired with an IDSpec ARCTIC Raman spectrometer (IDSpec, Beijing) at 633 nm laser. Electrochemical impedance spectroscopy (EIS), linear sweep voltammetry (LSV) and Tafel curves measurements were performed on an electrochemical workstation (CHI 660e). The frequency range of EIS spectra is from 100k Hz to 0.1 Hz. The scan rate of LSV curves and Tafel curves are 0.1 mV/s. Tafel curves measurements was conducted in a three-electrode configuration, in which saturated calomel electrode (SCE) was used as the reference electrode, Zn foils as the working electrode and the counter electrode, respectively.

A conductivity electrode was employed to investigate the ionic conductivity (σ) of different electrolytes. The corresponding ionic conductivity was calculated by

$$\sigma = \frac{K}{R} \tag{1}$$

where $\boldsymbol{K}$ is the cell constant (1.044 cm^{-1}), $\boldsymbol{R}$ is the bulk resistance.

Zn^{2+} transference number ($\boldsymbol{t_{Zn}^{2+}}$) was evaluated in Zn symmetric cell combined by EIS before and after the potential static, and calculated by the following equation:

$$t_{Zn^{2+}} = \frac{I_s(\Delta V - I_0 R_0)}{I_0(\Delta V - I_s R_s)} \tag{2}$$

where $\Delta \boldsymbol{V}$ is the applied polarization voltage (10 mV), $\boldsymbol{I_0}$ and $\boldsymbol{I_s}$ are the initial current and steady state current, respectively, $\boldsymbol{R_0}$ and $\boldsymbol{R_s}$ are the initial resistance and steady state resistance, respectively.

Texture coefficient of (hkl) facet ($\boldsymbol{TC_{(hkl)}}$) was calculated by:

$$TC_{(hkl)} = \frac{I_{(hkl)}/I_{0(hkl)}}{\sum I_{(hkl)}/I_{0(hkl)}} \times 100\% \tag{3}$$

Where $\boldsymbol{I_{(hkl)}}$ is the diffraction intensity of Zn (hkl) facet deposition layer, $\boldsymbol{I_{0(hkl)}}$ is the diffraction intensity of pristine Zn (hkl) facet.

3. Results and Discussion

3.1. Material synthesis and characterizations

The schematic synthesis of PAMPSZn hydrogel electrolyte is designed as Fig. 1. First, AMPSZn was prepared by ion exchange between AMPS and $3Zn(OH)_2•2ZnCO_3$. To confirm whether ion exchange was successful, pH of the AMPS and AMPSZn aqueous solutions were investigated by a pH meter, respectively. The pH value of 2.0 M AMPS aqueous solution is –0.30. After the ion exchange, the pH value of 1.0 M AMPSZn aqueous solution increases to 5.12, indicating that the protons of AMPS are exchanged by the Zn^{2+} of $3Zn(OH)_2•2ZnCO_3$ successfully. Then PAMPSZn hydrogel electrolyte was synthesized by free-radical polymerization from aqueous solution containing 1.0 M AMPSZn (based on the concentration of Zn^{2+}), 0.04 M MBAA and 0.001 M α-KGA. The obtained PAMPSZn hydrogel electrolyte is transparent as shown in Fig. S1. And it has certain mechanical properties, such as stretch, bend and twist (Fig. S2). FTIR spectra was tested to study the structure of PAMPSZn hydrogel electrolyte (Fig. S3). Compared with AMPS monomer, the absence of C=C absorption peak at 1614 cm^{-1} indicates that all AMPS monomers with C=C have polymerized in PAMPSZn hydrogel electrolyte. Scanning electron microscope (SEM) image and the corresponding EDS elemental mapping of Zn indicate that the Zn element distributes uniformly in PAMPSZn hydrogel electrolyte (Fig. S4).

The electrochemical properties of PAMPSZn hydrogel electrolyte are firstly verified. As shown in Fig. 2a, the PAMPSZn hydrogel electrolyte shows a high electrochemical stability window of ~2.4 V (vs. Zn/Zn^{2+}) by linear sweep voltammetry (LSV), which can meet almost all demands

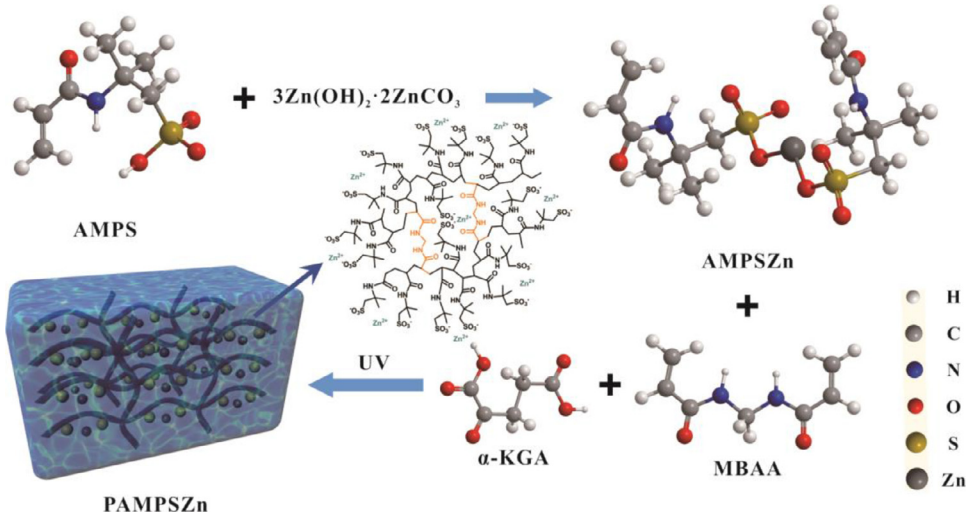

Fig. 1. Schematic synthesis of PAMPSZn hydrogel electrolyte.

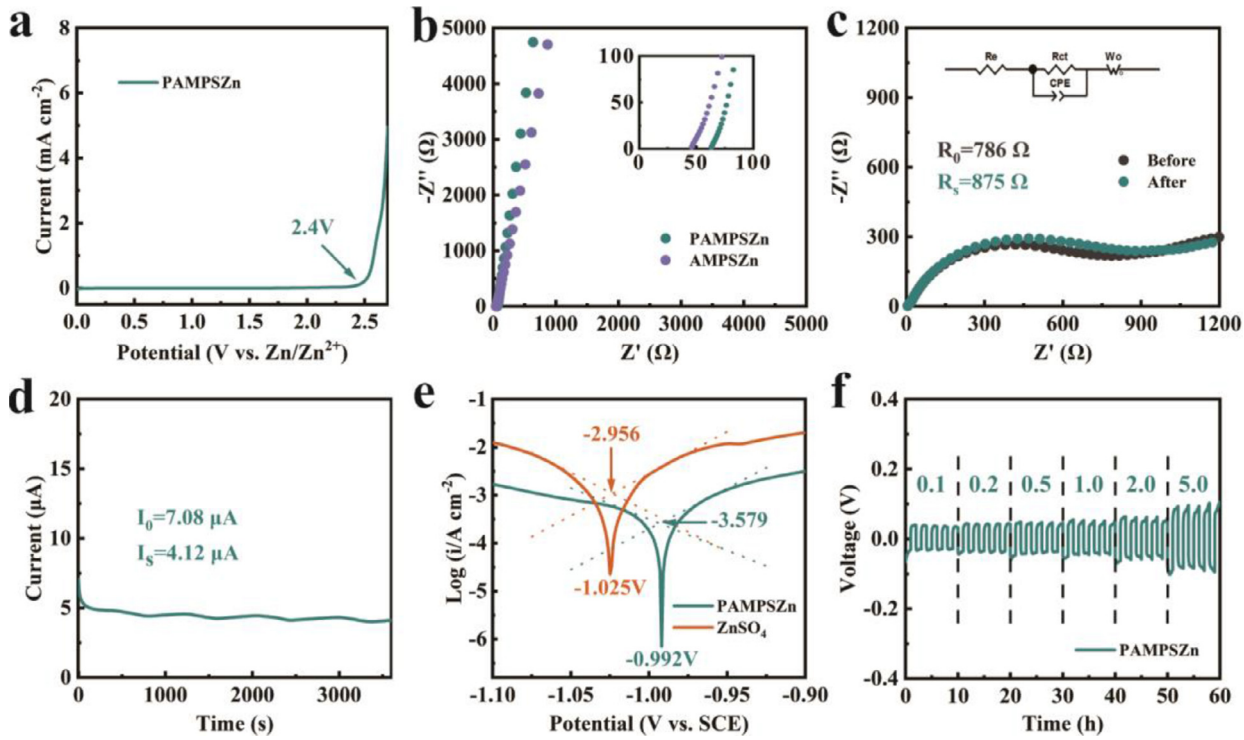

Fig. 2. (a) Electrochemical stability window of PAMPSZn hydrogel electrolyte. (b) EIS spectra of Zn/Zn symmetric cells with AMPSZn aqueous solution and PAMPSZn hydrogel electrolyte. (c) EIS spectra of Zn/Zn symmetric cell with PAMPSZn hydrogel electrolyte before and after polarization at an applied voltage of 10 mV and (d) the corresponding I-t curve. (e) Tafel curves of the 2.0 M $ZnSO_4$ aqueous electrolyte and PAMPSZn hydrogel electrolyte. (f) Voltage profile of Zn/PAMPSZn/Zn cell under various current densities.

of AZMBs system. To study the ion-conducting performance of the AMPSZn aqueous solution and PAMPSZn hydrogel electrolyte, the ionic conductivity is characterized by EIS (Fig. 2b). The AMPSZn aqueous solution exhibits a high ionic conductivity of 2.01×10^{-2} S cm^{-1} and only decreases to 1.56×10^{-2} S cm^{-1} in PAMPSZn hydrogel electrolyte, indicating the polymerization has mild impact on the ionic conductivity. Different concentrations of PAMPSZn hydrogel electrolyte are also characterized as shown in Fig. S5. Ionic conductivity first increases and then decreases as the concentration increases, and ionic conductivity is highest when the concentration of Zn^{2+} is 1.0 M. Zn^{2+} transference number (t_{Zn}^{2+}) of PAMPSZn hydrogel electrolyte is calculated by steady current method with a constant polarization potential of 10 mV and the result is demonstrated in Fig. 2c-d. The calculated Zn^{2+} transference number is 0.40, which is abnormal due to the local swing of the polyanionic chain [36]. In fact, since the proton is negligible (7.59×10^{-6} M), only Zn^{2+} are freely transmitted in PAMPSZn hydrogel electrolyte while the polyanionic chain with $-SO_3^-$ is fixed. Whereas, the ionic conductivity decreases owing to the process of which PAMPSZn hydrogel electrolyte is synthesized by AMPSZn aqueous solution. Therefore, PAMPSZn hydrogel electrolyte can be treated as single Zn^{2+} conductor. The effect of different electrolytes on the Zn corrosion is analyzed by Tafel curves (Fig. 2e). Compared with the $ZnSO_4$ aqueous electrolyte, the corrosion potential of Zn foil in PAMPSZn hydrogel electrolyte increases from -1.025 V to 0.992 V, indicating that it's more difficult to corrode Zn anodes. More importantly, the PAMPSZn hydrogel electrolyte shows a much weaker corrosion current (0.27 mA cm^{-2}) than the 2.0 M

$ZnSO_4$ aqueous electrolyte (1.11 mA cm^{-2}), revealing that the PAMPSZn hydrogel electrolyte is almost non-corrosive to zinc foil. Furthermore, the polarization voltage of Zn plating/stripping is investigated with a fixed time of 1h at different current densities from 0.1 to 5.0 mA cm^{-2} (Fig. 2f). When the current density increases from 0.1 mA cm^{-2} to 2.0 mA cm^{-2}, the polarization voltage is always below ~70 mV. And the polarization voltage is exclusively ~100 mV when the current density increases to 5.0 mA cm^{-2}. It demonstrates that the PAMPSZn hydrogel electrolyte is promising to be used for ARZBs over a wide range of current densities.

3.2. Electrochemical performance of aqueous zinc metal batteries

To investigate the long cycle stability of PAMPSZn hydrogel electrolyte, Zn/Zn symmetric cells were tested. Thickness tests were investigated in order to ensure the comparability between cells with different electrolytes (Fig. S6). And the results indicate that glass fiber and PAMPSZn hydrogel electrolyte, Zn/Zn symmetric cells with different electrolytes have almost the same thickness, respectively. The corresponding voltage profiles of Zn/Zn symmetric cells are presented as Fig. 3a. The Zn/Zn symmetric cell with PAMPSZn hydrogel electrolyte exhibits ultra-stable cycle performance, which can operate over 4500 h under a low polarization voltage of 100 mV at 1.0 mA cm^{-2} and 1.0 mAh cm^{-2}. Whereas, the Zn/Zn symmetric cell with $ZnSO_4$ aqueous electrolyte shows polarization increase at 114 h and suffers a short circuit at 139 h. In order to prove that the plating/stripping of Zn with PAMPSZn hydrogel electrolyte can operate stably over a wide range of current densities, Zn/Zn symmetric cells at different current densities are investigated. As a result, the Zn/Zn symmetric cell with PAMPSZn hydrogel electrolyte can operate for 1800 h and 800h under a polarization voltage of 100 mV at current densities of 0.1 mA cm^{-2} (Fig. S7) and 0.5 mA cm^{-2} (Fig. S8), respectively. Whereas, the Zn/Zn symmetric cell with $ZnSO_4$ aqueous electrolyte shows short circuit after only 155 h at 0.1 mA cm^{-2} and polarization increase after only 130 h at a current density of 0.5 mA cm^{-2}, respectively. Even when the current density increases to 5.0 mA cm^{-2}, the Zn/Zn symmetric cell can still operate stably over 100 h (Fig. S9). This ultra-stable lifespan remarkably outperforms all of reported Zn/Zn symmetric cells at the similar current density and specific capacity (Fig. 3h), corroborating the enormous promising prospect of PAMPSZn hydrogel electrolyte in AZMBs.

Reversibility is equally important for the cells operation. Zn/Cu asymmetric cells with different electrolytes were assembled and tested to verify the cycle reversibility of Zn plating/stripping. The corresponding cycle performance are presented as Fig. 3b. The Zn/Cu asymmetric cell with

PAMPSZn hydrogel electrolyte exhibits high reversible electrochemical performance, whose average coulombic efficiency can maintain at 99.3% after 400 cycles. Whereas, the Zn/Cu asymmetric cell with $ZnSO_4$ aqueous electrolyte can only operate 28 cycles with a low average coulombic efficiency of 74.6%. The side reaction levels of cell with different electrolyte can be demonstrated by coulombic efficiency of first cycle. The Zn/Cu asymmetric cell with PAMPSZn hydrogel electrolyte has a higher initial coulombic efficiency of 87.5% than that with $ZnSO_4$ aqueous electrolyte (67.3%), indicating less side reactions in the Zn/Cu asymmetric cell with PAMPSZn hydrogel electrolyte. Similar results are also obtained at 1.0 mA cm^{-2} and 1.0 mAh cm^{-2} (Fig. S10). Moreover, Fig. 3c shows that the Zn/Cu asymmetric cell with PAMPSZn hydrogel electrolyte retains a low and stable overpotential over long-term operation.

Zn/V_2O_5 cells (Fig. 3g) were assembled to further evaluate the practical applications of the PAMPSZn hydrogel electrolyte. V_2O_5•$1.6H_2O$ cathode materials were synthesized successfully by a simple hydrothermal method according to reference [45]. And the corresponding SEM images, TEM images, XRD pattern and Raman spectra were employed to investigate the structure of V_2O_5•$1.6H_2O$ cathode. The synthesized V_2O_5•$1.6H_2O$ presents a nanoribbon structure (Fig. S11a-b). And the corresponding EDS elemental mapping indicates that the distribution of oxygen and vanadium in the cathode material is consistent (Fig. S11c-d). The TEM images of nanoribbon show the interplanar distance as 0.193 nm corresponding to (006) facet of V_2O_5•$1.6H_2O$ cathode (Fig. S11c-d). XRD pattern shows six obvious diffraction peaks at 7.6°, 23.3°, 30.7° 38.8°, 47.3° and 50.6°, indexed to (001), (003), (004), (005), (006) and (007) facets of V_2O_5•$1.6H_2O$ (JCPDS NO: 40-1296), respectively (Fig. S12a). And the Raman spectra shows five strong characteristic peaks at 140, 192, 283, 405 and 690 cm^{-1} for both the V_2O_5·$1.6H_2O$ and pristine V_2O_5, demonstrating the V_2O_5·$1.6H_2O$ nanoribbons have the similar V-O vibration behavior with the pristine V_2O_5 (Fig. S12b). The Zn/V_2O_5 cell with PAMPSZn hydrogel electrolyte shows a high capacity retention of 80.2% (280.7 mAh g^{-1}, initial specific capacity is 350.0 mAh g^{-1}) at 0.5 A g^{-1} after 400 cycles. And the initial coulombic efficiency of Zn/V_2O_5 cell PAMPSZn hydrogel electrolyte is 97.9%, which is much higher than $ZnSO_4$ aqueous electrolyte (85.3%). Whereas, the Zn/V_2O_5 cell with $ZnSO_4$ aqueous electrolyte remains only 10.8% capacity retention (34.0 mAh g^{-1}, initial specific capacity is 219.6 mAh g^{-1}) at a current density of 0.5 A g^{-1} after 400 cycles. The Zn/V_2O_5 cell can operate more than 2000 cycles with nearly 100% coulombic efficiency and the short-circuit induced failure doesn't occur, indicating PAMPSZn hydrogel electrolyte possesses ultra-stable and highly reversible electrochemical performance (Fig. S13). In addition, Fig. 3e demonstrates that the Zn/V_2O_5 cell with PAMPSZn hydrogel electrolyte maintains a relatively stable charging and discharging platform, which reveals the Zn/V_2O_5 cells possess superior reversibility. Furthermore, the Zn/V_2O_5 cells with PAMPSZn hydrogel electrolyte delivers exceptional rate performance from 0.1 A g^{-1} to 2.0 A g^{-1} as shown in Fig. 3f. The Zn/V_2O_5 cells with PAMPSZn hydrogel electrolyte show a high initial capacity of 438.9 mAh g^{-1} at 0.1 A g^{-1}. Even at a high current density of 2.0 A g^{-1}, it still delivers a significantly capacity of 288.2 mAh g^{-1}, remaining a high capacity retention of 65.7% compared with that at 0.1 A g^{-1}. To investigate the reason of the Zn/V_2O_5 cell degradation, XRD and SEM were employed to study the changes of V_2O_5 electrodes before and after repeated charge and discharge. XRD patterns of cycled V_2O_5 cathode electrodes show that the cathode electrode with $ZnSO_4$ electrolyte has more impurity diffraction peaks than PAMPSZn hydrogel electrolyte (Fig. S14). The topography of cycled V_2O_5 cathode electrode with PAMPSZn hydrogel electrolyte is similar with pristine V_2O_5 cathode electrode, whereas the V_2O_5 cathode electrode with $ZnSO_4$ electrolyte has collapsed, demonstrating that PAMPSZn hydrogel electrolyte alleviates the collapse of the cathode materials more effectively than $ZnSO_4$ electrolyte (Fig. S15). These results indicate a promising future of PAMPSZn hydrogel electrolyte in AZMBs applications.

3.3. Mechanism schematic

To certificate the short-circuit induced failure mechanism of AZMBs, the three-dimensional topography of Zn anodes in the Zn/Zn symmetric cells with different electrolytes after 10th, 20th and 50th cycles are firstly observed by CLMS (Fig. 4a-f). The pristine Zn is flat as shown in Fig. S16. Obvious peaks and valleys can be observed on the Zn anodes in the Zn/Zn symmetric cells with $ZnSO_4$ aqueous electrolyte as Fig. 4a-c shown. And the surface of Zn anodes will become rougher and rougher as the cycle number increases. Whereas, the roughness of the Zn anodes surface in the Zn/Zn symmetric cells with PAMPSZn hydrogel electrolyte has only changed slightly when the cycle number increases from 10 cycles to 50 cycles according to Fig. 4d-f. In order to quantitatively describe the surface topography, surface roughness is calculated by VK-X series. The surface roughness of Zn anodes in the Zn/Zn symmetric cells with PAMPSZn hydrogel electrolyte is much smaller than the $ZnSO_4$ aqueous electrolyte as Table S1 shown.

These results demonstrate that it's more likely to cause short-circuit induced failure in Zn/Zn symmetric cells with $ZnSO_4$ aqueous electrolyte due to uneven topography of Zn metal anodes.

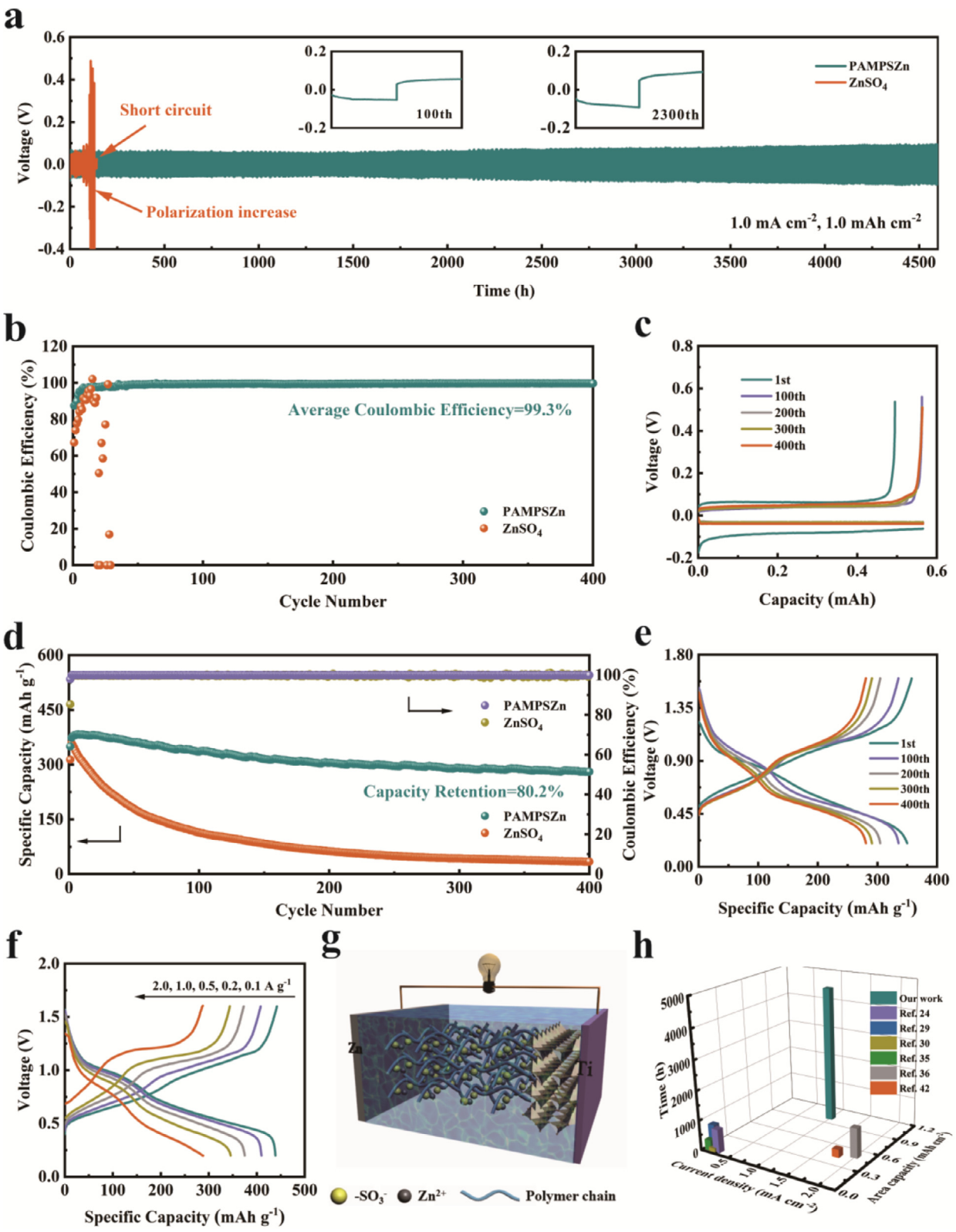

Fig. 3. (a) Voltage profile of Zn/Zn symmetric cells with different electrolytes. The insets are the voltage profile of 100th and 2300th cycle, respectively. (b) Cycle performance of Zn/Cu cells with different electrolytes. (c) Voltage/capacity plots of Zn/Cu cell with PAMPSZn hydrogel electrolyte. (d) Cycle performance of Zn/V_2O_5 cells with different electrolytes. (e) Voltage/capacity plots of Zn/V_2O_5 cell with PAMPSZn hydrogel electrolyte. (f) Rate performance of Zn/V_2O_5 cell with PAMPSZn hydrogel electrolyte. (g) 3D models of Zn/V_2O_5 cells with PAMPSZn hydrogel electrolyte. (h) Comparison of electrochemical properties of the reported Zn/Zn symmetric cells.

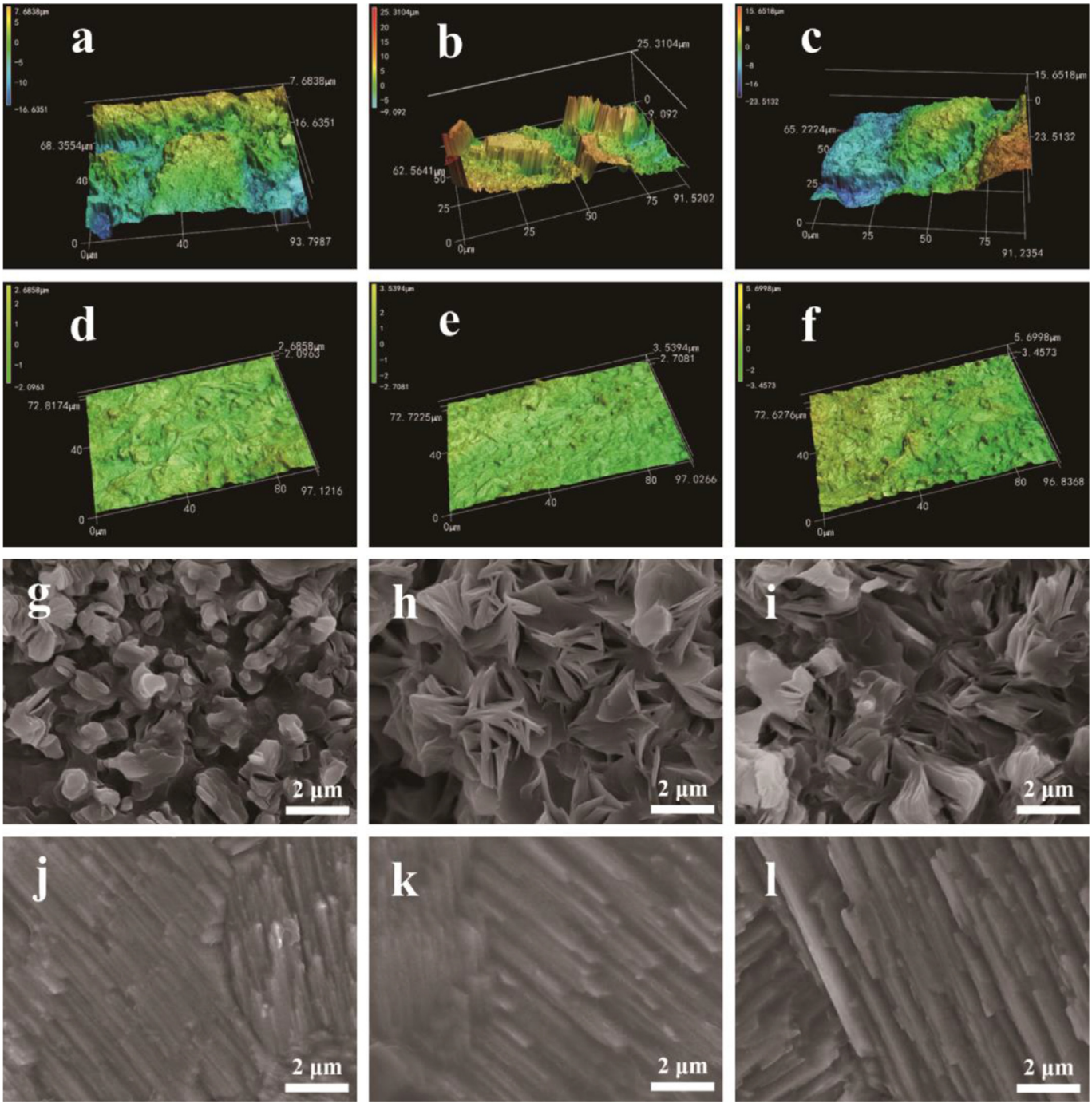

Fig. 4. CLMS images of Zn anodes in the Zn/Zn symmetric cell after several cycles with (a)-(c) $ZnSO_4$ aqueous electrolyte and (d)-(f) PAMPSZn hydrogel electrolyte at 1.0 mA cm^{-2} and 1.0 mAh cm^{-2}. (a), (d) 10 cycles; (b), (e)20 cycles; (c), (f) 50 cycles. High magnification SEM images of Zn anodes in the Zn/Zn symmetric cells after several cycles with (g)-(i) $ZnSO_4$ aqueous electrolyte and (j)-(l) PAMPSZn hydrogel electrolyte at 1.0 mA cm^{-2} and 1.0 mAh cm^{-2}. (g), (j) 10 cycles; (h), (k) 20 cycles; (i), (l) 50 cycles.

To further confirm the short-circuit failure mechanism of AZMBs, SEM is employed to observe the surface topography of Zn anodes in Zn/Zn symmetric cells with different electrolytes after 10, 20 and 50 cycles, respectively. The surface topography of pristine Zn is characterized as Fig. S17 shown. As shown in Fig. 4g-l and Fig.S18a-c, the initial small dendrite tips on Zn foil surface after 10 cycles gradually become coarse flaky dendrites in the $ZnSO_4$ aqueous electrolyte when the charge/discharge cycle increases to 50 cycles. In PAMPSZn hydrogel electrolyte, it is interesting to find that the Zn foil surface forms uniform nanowires after 10 cycles (Fig. S19).

The nanowires become thicker after 50 cycles, but still maintain a uniform appearance (Fig. 4j-l and Fig.S18d-f). Similar results were obtained at different current densities and area capacities as shown in Fig. S20. In addition, the Zn morphology of cycled Zn/V_2O_5 cells with different electrolytes was also observed (Fig. S21). Although there is a little difference from the Zn morphology in Zn symmetric cells [46], uniform nanowires are also observed in Zn/V_2O_5 cells with PAMPSZn hydrogel electrolyte. And the zinc anodes surface of Zn/V_2O_5 cells using PAMPSZn hydrogel electrolyte is smoother than that of $ZnSO_4$ electrolyte. These results indicate that different from $ZnSO_4$ aqueous elec-

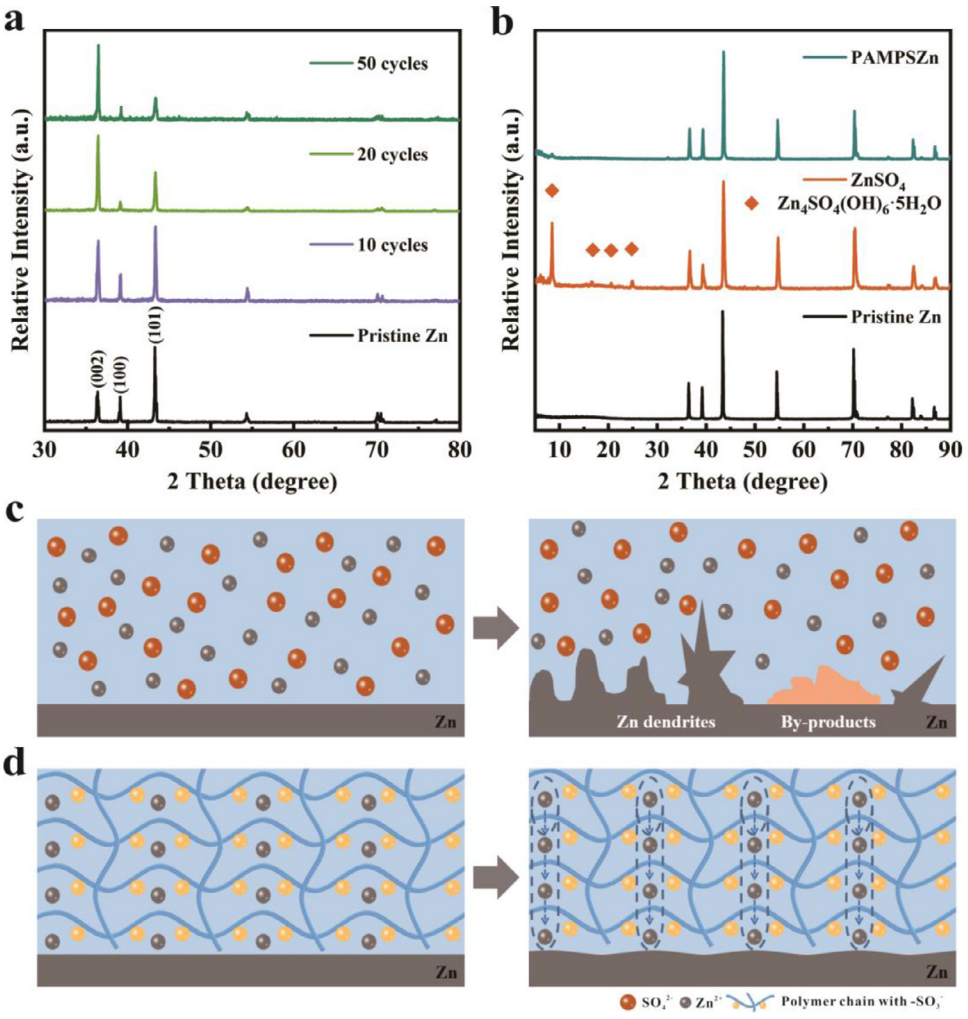

Fig. 5. (a) GIXRD patterns of pristine Zn and Zn anodes in the Zn/Zn symmetric cell after 10, 20, 50 cycles at 1.0 mA cm^{-2} and 1.0 mAh cm^{-2}. (b) XRD patterns of pristine Zn foil and Zn anodes in the Zn/Zn symmetric cells with different electrolyte after 3 cycles at 1.0 mA cm^{-2} and 1.0 mAh cm^{-2}. (c)-(d) The mechanism of Zn deposition/stripping with (c) $ZnSO_4$ aqueous electrolyte and (d) PAMPSZn hydrogel electrolyte.

trolyte, the PAMPSZn hydrogel electrolyte is beneficial to the uniform plating/stripping of Zn.

To investigate the evolution of crystal structure about nanowires deposition layers, grazing incidence X-ray Diffraction (GIXRD) is employed to analyze the surface layer of Zn anodes in Zn/Zn symmetric cells with PAMPSZn hydrogel electrolyte after several cycles. The results (Fig. 5a) show that the diffraction peak of (101) facet becomes weaker and weaker while (002) facet becomes stronger and stronger, demonstrating that Zn^{2+} trend to deposit along (002) facet. To confirm the high preferred orientation deposition of Zn^{2+}, texture coefficient of (hkl) facet ($TC_{(hkl)}$) is calculated on the basis of (002), (100) and (101) facets (Table S2). The texture coefficient of (002) facet increases from 0.4928 to 0.7444 while that of (001) decreases from 0.2516 to 0.0928, confirming that the deposition of Zn^{2+} has a high preferred orientation in PAMPSZn hydrogel electrolyte.

For the polarization induced failure mechanism of AZMBs, the XRD pattern (Fig. 5b) of Zn foil in Zn/Zn symmetric cell with $ZnSO_4$ aqueous electrolyte shows obvious impurity peaks at 8.5°, 16.8°, 20.6° and 24.8°, which are attributed to $Zn_4SO_4(OH)_6 \bullet 5H_2O$ (JCPDS NO: 39–0688) by-products by a serious side reaction between Zn anode and SO_4^{2-}:

$$4Zn^{2+} + 6OH^- + SO_4^{2-} + 5H_2O \rightarrow Zn_4(OH)_6SO_4 \cdot 5H_2O \quad (4)$$

Whereas, the XRD pattern of Zn foil in Zn/Zn symmetric cell with PAMPSZn hydrogel electrolyte shows no obvious diffraction peaks except Zinc metal peaks, which demonstrate that PAMPSZn hydrogel electrolyte alleviates the side reactions of the interface between Zn and electrolyte effectively.

The mechanism of Zn deposition/stripping with different electrolytes can be summarized according to the previous results and analysis. For the $ZnSO_4$ aqueous electrolyte, a large amount of movable SO_4^{2-} cations will keep in contact with Zn anode under the effect of electric field, which causes severe side reactions and produces a lot of by-products. By products without the ability to conduct Zn^{2+} cover the surface of Zn anode, resulting the polarization increase.

Meanwhile, freely transmitted Zn^{2+} tend to accumulate on the small tips at the surface of Zn metal anodes under applied voltage. Zn dendrites will form and grow due to the uneven interfacial electric field and ion concentration [47]. Whereas for PAMPSZn hydrogel electrolyte, polyanionic chain with $-SO_3^-$ is fixed in PAMPSZn hydrogel electrolyte, which reduces the concentration polarization of anions and alleviates side reactions because of the limited contact between $-SO_3^-$ and the surface of Zn metal anode. Simultaneously, Zn^{2+} can only transport in uniform Zn^{2+} transport channels under the restriction of polyanionic chain, which achieves uniform deposition/stripping on the surface of zinc metal anodes. As a result, AZMBs with the PAMPSZn hydrogel electrolyte delivers an ultra-stable and high reversible electrochemical performance.

4. Conclusion

In summary, the PAPMSZn hydrogel electrolyte was firstly designed and synthesized for AZMBs by ion exchange and free-radical polymerization. It alleviates the side reactions of the interface between Zn and electrolyte effectively because the polyanionic chain with $-SO_3^-$

is fixed in PAMPSZn hydrogel electrolyte. Meanwhile, Zn^{2+} can plating/stripping uniformly on the surface of zinc metal anodes because of the restricted and uniform Zn^{2+} transport channels. Consequently, ultra-stable Zn plating/stripping was achieved over 4500 h at 1.0 mA cm^{-2}. Excellent cycle stability and high reversibility were also achieved in the Zn/Cu cells and Zn/V_2O_5 cells with the PAMPSZn hydrogel electrolyte. Furthermore, the deposition of Zn accompanied by high preferred orientation owing to the PAMPSZn hydrogel electrolyte. This work sheds lights on the high performance AZMBs based on hydrogel electrolyte.

Credit Author Statement

Jianlong Cong completes the main work of the study and prepares the manuscript.

Xiu Shen takes part in the design of experiments and partial work of the study.

Zhipeng Wen, Xin Wang and Longqing Peng take part in the discussion of involved mechanism.

Jing Zeng and Jinbao Zhao are as supervisors to the study.

Declaration of Competing Interest

The authors declare that they have no known competing financial interests or personal relationships that could have appeared to influence the work reported in this paper.

Acknowledgements

This research was supported by the National Natural Science Foundation of China (Grant Numbers 21875198 and 22005257) and Natural Science Foundation of Fujian Province of China (No. 2020J05009).

Supplementary materials

Supplementary material associated with this article can be found, in the online version, at doi:10.1016/j.ensm.2020.11.041.

References

[1] M. Li, J. Lu, Z.W. Chen, K. Amine, 30 Years of Lithium-Ion Batteries, Adv. Mater. 30 (2018).
[2] R. Schmuch, R. Wagner, G. Hörpel, T. Placke, M. Winter, Performance and cost of materials for lithium-based rechargeable automotive batteries, Nat. Energy 3 (2018) 267–278.
[3] X. Feng, M. Ouyang, X. Liu, L. Lu, Y. Xia, X. He, Thermal runaway mechanism of lithium ion battery for electric vehicles: A review, Energy Storage Mater 10 (2018) 246–267.
[4] Y. Cui, Q. Zhang, J. Wu, X. Liang, A.P. Baker, D. Qu, H. Zhang, H. Zhang, X. Zhang, Developing porous carbon with dihydrogen phosphate groups as sulfur host for high performance lithium sulfur batteries, J. Power Sources 378 (2018) 40–47.
[5] G. Qian, X. Liao, Y. Zhu, F. Pan, X. Chen, Y. Yang, Designing Flexible Lithium-Ion Batteries by Structural Engineering, ACS Energy Lett 4 (2019) 690–701.
[6] J.B. Goodenough, K.S. Park, The Li-ion rechargeable battery: a perspective, J. Am. Chem. Soc. 135 (2013) 1167–1176.
[7] Z. Guo, Y. Zhao, Y. Ding, X. Dong, L. Chen, J. Cao, C. Wang, Y. Xia, H. Peng, Y. Wang, Multi-functional Flexible Aqueous Sodium-Ion Batteries with High Safety, Chem 3 (2017) 348–362.
[8] J.M. Tarascon, M. Armand, Issues and challenges facing rechargeable lithium batteries, Nature 414 (2001) 359–367.
[9] Z. Zhang, S. Dong, Z. Cui, A. Du, G. Li, G. Cui, Rechargeable Magnesium Batteries using Conversion-Type Cathodes: A Perspective and Minireview, Small Methods 2 (2018).
[10] W. Wang, J. Zhou, Z. Wang, L. Zhao, P. Li, Y. Yang, C. Yang, H. Huang, S. Guo, Short--Range Order in Mesoporous Carbon Boosts Potassium-Ion Battery Performance, Adv. Energy Mater. 8 (2018).
[11] P.K. Nayak, L. Yang, W. Brehm, P. Adelhelm, From Lithium-Ion to Sodium-Ion Batteries: Advantages, Challenges, and Surprises, Angew. Chem., Int. Ed. 57 (2018) 102–120.
[12] G. Fang, J. Zhou, A. Pan, S. Liang, Recent Advances in Aqueous Zinc-Ion Batteries, ACS Energy Lett 3 (2018) 2480–2501.
[13] F. Wan, L. Zhang, X. Wang, S. Bi, Z. Niu, J. Chen, An Aqueous Rechargeable Zinc-Organic Battery with Hybrid Mechanism, Adv. Funct. Mater. 28 (2018).
[14] F. Ming, H. Liang, Y. Lei, S. Kandambeth, M. Eddaoudi, H.N. Alshareef, Layered MgxV2O5•nH2O as Cathode Material for High-Performance Aqueous Zinc Ion Batteries, ACS Energy Lett 3 (2018) 2602–2609.
[15] B. Jiang, C. Xu, C. Wu, L. Dong, J. Li, F. Kang, Manganese Sesquioxide as Cathode Material for Multivalent Zinc Ion Battery with High Capacity and Long Cycle Life, Electrochim. Acta 229 (2017) 422–428.
[16] Y. Cai, F. Liu, Z. Luo, G. Fang, J. Zhou, A. Pan, S. Liang, Pilotaxitic Na1.1V3O7.9 nanoribbons/graphene as high-performance sodium ion battery and aqueous zinc ion battery cathode, Energy Storage Mater 13 (2018) 168–174.
[17] B. Lee, H.R. Seo, H.R. Lee, C.S. Yoon, J.H. Kim, K.Y. Chung, B.W. Cho, S.H. Oh, Critical Role of pH Evolution of Electrolyte in the Reaction Mechanism for Rechargeable Zinc Batteries, ChemSusChem 9 (2016) 2948–2956.
[18] Q. Zhang, J. Luan, Y. Tang, X. Ji, H. Wang, Interfacial Design of Dendrite-Free Zinc Anodes for Aqueous Zinc-Ion Batteries, Angew. Chem., Int. Ed. 59 (2020) 13180–13191.
[19] Q. Zhang, J. Luan, X. Huang, Q. Wang, D. Sun, Y. Tang, X. Ji, H. Wang, Revealing the role of crystal orientation of protective layers for stable zinc anode, Nat. Commun. 11 (2020) 3961.
[20] R. Yuksel, O. Buyukcakir, W.K. Seong, R.S. Ruoff, Metal-Organic Framework Integrated Anodes for Aqueous Zinc-Ion Batteries, Adv. Energy Mater. 10 (2020).
[21] J. Shin, J. Lee, Y. Park, J.W. Choi, Aqueous zinc ion batteries: focus on zinc metal anodes, Chem. Sci. 11 (2020) 2028–2044.
[22] H. Qiu, X. Du, J. Zhao, Y. Wang, J. Ju, Z. Chen, Z. Hu, D. Yan, X. Zhou, G. Cui, Zinc anode-compatible in-situ solid electrolyte interphase via cation solvation modulation, Nat. Commun. 10 (2019) 5374.
[23] K. Zhao, C. Wang, Y. Yu, M. Yan, Q. Wei, P. He, Y. Dong, Z. Zhang, X. Wang, L. Mai, Ultrathin Surface Coating Enables Stabilized Zinc Metal Anode, Adv. Mater. Interfaces 5 (2018).
[24] L. Kang, M. Cui, F. Jiang, Y. Gao, H. Luo, J. Liu, W. Liang, C. Zhi, Nanoporous CaCO3 Coatings Enabled Uniform Zn Stripping/Plating for Long-Life Zinc Rechargeable Aqueous Batteries, Adv. Energy Mater. 8 (2018).
[25] Z. Zhao, J. Zhao, Z. Hu, J. Li, J. Li, Y. Zhang, C. Wang, G. Cui, Long-life and deeply rechargeable aqueous Zn anodes enabled by a multifunctional brightener-inspired interphase, Energy Environ. Sci. 12 (2019) 1938–1949.
[26] X. Liu, F. Yang, W. Xu, Y. Zeng, J. He, X. Lu, Zeolitic Imidazolate Frameworks as Zn2+ Modulation Layers to Enable Dendrite-Free Zn Anodes, Adv. Sci. (2020).
[27] S.B. Wang, Q. Ran, R.Q. Yao, H. Shi, Z. Wen, M. Zhao, X.Y. Lang, Q. Jiang, Lamella–nanostructured eutectic zinc-aluminum alloys as reversible and dendrite-free anodes for aqueous rechargeable batteries, Nat. Commun. 11 (2020) 1634.
[28] J.X. Zheng, Q. Zhao, T. Tang, J.F. Yin, C.D. Quilty, G.D. Renderos, X.T. Liu, Y. Deng, L. Wang, D.C. Bock, C. Jaye, D.H. Zhang, E.S. Takeuchi, K.J. Takeuchi, A.C. Marschilok, L.A. Archer, Reversible epitaxial electrodeposition of metals in battery anodes, Science 366 (2019) 645-+.
[29] N. Zhang, F.Y. Cheng, Y.C. Liu, Q. Zhao, K.X. Lei, C.C. Chen, X.S. Liu, J. Chen, Cation-Deficient Spinel ZnMn2O4 Cathode in Zn(CF3SO3)(2) Electrolyte for Rechargeable Aqueous Zn-Ion Battery, J. Am. Chem. Soc. 138 (2016) 12894–12901.
[30] F. Wang, O. Borodin, T. Gao, X. Fan, W. Sun, F. Han, A. Faraone, J.A. Dura, K. Xu, C. Wang, Highly reversible zinc metal anode for aqueous batteries, Nat. Mater. 17 (2018) 543–549.
[31] C. Zhang, J. Holoubek, X. Wu, A. Daniyar, L. Zhu, C. Chen, D.P. Leonard, I.A. Rodriguez-Perez, J.X. Jiang, C. Fang, X. Ji, A ZnCl2 water-in-salt electrolyte for a reversible Zn metal anode, Chem Commun (Camb) 54 (2018) 14097–14099.
[32] J. Hao, J. Long, B. Li, X. Li, S. Zhang, F. Yang, X. Zeng, Z. Yang, W.K. Pang, Z. Guo, Toward High-Performance Hybrid Zn-Based Batteries via Deeply Understanding Their Mechanism and Using Electrolyte Additive, Adv. Funct. Mater. 29 (2019).
[33] Q. Zhang, J. Luan, L. Fu, S. Wu, Y. Tang, X. Ji, H. Wang, The Three-Dimensional Dendrite-Free Zinc Anode on a Copper Mesh with a Zinc-Oriented Polyacrylamide Electrolyte Additive, Angew. Chem., Int. Ed. 58 (2019) 15841–15847.
[34] K.E. Sun, T.K. Hoang, T.N. Doan, Y. Yu, X. Zhu, Y. Tian, P. Chen, Suppression of Dendrite Formation and Corrosion on Zinc Anode of Secondary Aqueous Batteries, ACS Appl Mater Interfaces 9 (2017) 9681–9687.
[35] Z.Q. Wang, J.T. Hu, L. Han, Z.J. Wang, H.B. Wang, Q.H. Zhao, J.J. Liu, F. Pan, A MOF-based single-ion Zn2+ solid electrolyte leading to dendrite-free rechargeable Zn batteries, Nano Energy 56 (2019) 92–99.
[36] Y. Cui, Q. Zhao, X. Wu, Z. Wang, R. Qin, Y. Wang, M. Liu, Y. Song, G. Qian, Z. Song, L. Yang, F. Pan, Quasi-solid single Zn-ion conductor with high conductivity enabling dendrite-free Zn metal anode, Energy Storage Mater 27 (2020) 1–8.
[37] A. Naveed, H. Yang, J. Yang, Y. Nuli, J. Wang, Highly Reversible and Rechargeable Safe Zn Batteries Based on a Triethyl Phosphate Electrolyte, Angew. Chem., Int. Ed. 58 (2019) 2760–2764.
[38] K. Leng, G. Li, J. Guo, X. Zhang, A. Wang, X. Liu, J. Luo, A Safe Polyzwitterionic Hydrogel Electrolyte for Long-Life Quasi-Solid State Zinc Metal Batteries, Adv. Funct. Mater. 30 (2020).
[39] S. Huang, F. Wan, S. Bi, J. Zhu, Z. Niu, J. Chen, A Self-Healing Integrated All-in-One Zinc-Ion Battery, Angew. Chem., Int. Ed. 58 (2019) 4313–4317.
[40] S. Zhang, N. Yu, S. Zeng, S. Zhou, M. Chen, J. Di, Q. Li, An adaptive and stable bio-electrolyte for rechargeable Zn-ion batteries, J. Mater. Chem. A 6 (2018) 12237–12243.
[41] Q. Zhang, C. Li, Q. Li, Z. Pan, J. Sun, Z. Zhou, B. He, P. Man, L. Xie, L. Kang, X. Wang, J. Yang, T. Zhang, P.P. Shum, Q. Li, Y. Yao, L. Wei, Flexible and High-Voltage Coaxial-Fiber Aqueous Rechargeable Zinc-Ion Battery, Nano Lett. 19 (2019) 4035–4042.

[42] Y. Tang, C. Liu, H. Zhu, X. Xie, J. Gao, C. Deng, M. Han, S. Liang, J. Zhou, Ion–confinement effect enabled by gel electrolyte for highly reversible dendrite-free zinc metal anode, Energy Storage Mater 27 (2020) 109–116.
[43] Z. Liu, D. Wang, Z. Tang, G. Liang, Q. Yang, H. Li, L. Ma, F. Mo, C. Zhi, A mechanically durable and device-level tough Zn-MnO2 battery with high flexibility, Energy Storage Mater 23 (2019) 636–645.
[44] L. Ma, S. Chen, N. Li, Z. Liu, Z. Tang, J.A. Zapien, S. Chen, J. Fan, C. Zhi, Hydrogen-Free and Dendrite-Free All-Solid-State Zn-Ion Batteries, Adv. Mater. 32 (2020).
[45] X. Wang, L. Ma, P. Zhang, H. Wang, S. Li, S. Ji, Z. Wen, J. Sun, Vanadium pentoxide nanosheets as cathodes for aqueous zinc-ion batteries with high rate capability and long durability, Appl. Surf. Sci. 502 (2020).
[46] Q. Yang, Q. Li, Z. Liu, D. Wang, Y. Guo, X. Li, Y. Tang, H. Li, B. Dong, C. Zhi, Dendrites in Zn-Based Batteries, Adv. Mater. (2020) e2001854.
[47] Q. Yang, G.J. Bang, Y. Guo, Z.X. Liu, B.X. Yon, D.H. Wang, Z.D. Huang, X.L. Li, J. Fan, C.Y. Zhi, Do Zinc Dendrites Exist in Neutral Zinc Batteries: A Developed Electrohealing Strategy to In Situ Rescue In-Service Batteries, Adv. Mater. 31 (2019).